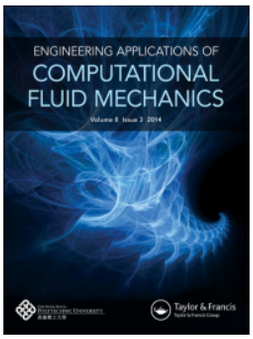

Taylor & Francis
Taylor & Francis Group

Engineering Applications of Computational Fluid Mechanics

ISSN: (Print) (Online) Journal homepage: www.tandfonline.com/journals/tcfm20

Flow characteristics analysis of an ultrathin forward-curved multi-blade centrifugal fan

Weiwei Liao, Yijun Mao & Xiaobing Luo

To cite this article: Weiwei Liao, Yijun Mao & Xiaobing Luo (2025) Flow characteristics analysis of an ultrathin forward-curved multi-blade centrifugal fan, Engineering Applications of Computational Fluid Mechanics, 19:1, 2434028, DOI: 10.1080/19942060.2024.2434028

To link to this article: https://doi.org/10.1080/19942060.2024.2434028

Published online: 12 Dec 2024.

ENGINEERING APPLICATIONS OF COMPUTATIONAL FLUID MECHANICS
2025, VOL. 19, NO. 1, 2434028
https://doi.org/10.1080/19942060.2024.2434028

Flow characteristics analysis of an ultrathin forward-curved multi-blade centrifugal fan

Weiwei Liao[a], Yijun Mao[b] and Xiaobing Luo[a]

[a]School of Energy and Power Engineering, Huazhong University of Science and Technology, Wuhan, People's Republic of China; [b]School of Aerospace Engineering, Huazhong University of Science and Technology, Wuhan, People's Republic of China

ABSTRACT

The ultrathin centrifugal fan, widely utilised in compact electronic devices such as laptops, is characterised by numerous forward-curved blades that generate high static pressure and flow rates. Despite its widespread application, the flow dynamics of ultrathin centrifugal fans remain insufficiently explored. In large-scale centrifugal turbomachinery, boundary layer thickness is typically negligible, with flow separation being the primary contributor to flow losses. However, the loss mechanisms in ultrathin centrifugal fans are not yet well understood. This study addresses these gaps by investigating entropy production associated with various flow processes, decomposing entropy generation into components related to molecular viscosity and eddy viscosity. Large Eddy Simulation (LES) is employed to analyze the turbulent characteristics of ultrathin centrifugal fans. The findings indicate that the boundary layer thickness, constituting approximately 10% of the volute height, is substantial. Viscous dissipation within the boundary layer generates 2.85×10^{-4} W/K of entropy, whereas flow separation contributes 1.16×10^{-5} W/K, underscoring the significant impact of the boundary layer on the fan's operational efficiency. To further investigate the turbulence characteristics, hot-wire anemometry measurements were conducted to obtain the turbulent energy spectrum. Moreover, the turbulence scale and pressure fluctuations derived from simulation results were analyzed in the frequency domain, revealing that low-frequency components are linked to blade surfaces, while high-frequency components are associated with the volute shell. The insights gained from this flow field analysis can inform the design of more efficient and quieter cooling fans.

ARTICLE HISTORY
Received 11 June 2024
Accepted 20 October 2024

KEYWORDS
Flow separation; boundary layer; entropy production; large eddy simulation

Nomenclature

k_{sgs}	subgrid turbulent kinetic energy, m^2/s^2
k_{res}	resolved turbulent kinetic energy, m^2/s^2
L_{int}	integral length scale, m
R_{spa}	spatial resolution
S_{mean}	mean flow induced entropy production, W/K
S_{tur}	turbulence induced entropy production, W/K
S_{vis}	viscosity induced entropy production, W/K
$S_{eddy-vis}$	eddy-viscosity induced entropy production, W/K
T	temperature, K
T_{int}	integral time scale, s
u,v,w	three velocity components, m/s
$\bar{u}$, $\bar{v}$, $\bar{w}$	time-averaged velocity components, m/s
u', v', w'	fluctuation components of velocity, m/s
x, y, z	three directions, m
ϵ	dissipation rate, m^2/s^3
μ	dynamic viscosity, Pa · s
μ_{eff}	effective viscosity, Pa · s
μ_t	eddy viscosity, Pa · s
ρ	air density, kg/m^3
τ_{ij}	subgrid stress, Pa

1. Introduction

The ultrathin centrifugal fan is widely employed for forced cooling in compact electronic devices. Due to installation constraints, the axial dimension of these fans is typically restricted to less than 1 cm, limiting their capacity for mechanical work. To compensate for this limitation, ultrathin centrifugal fans often utilise a forward-curved, multi-blade design, which helps generate a strong adverse pressure gradient and a high flow rate. Additionally, these small-scale fans are designed to operate at high revolutions per minute (RPM) to maximise heat dissipation from the heat sink. These design features distinguish ultrathin centrifugal fans from their industrial counterparts. Therefore, a comprehensive

CONTACT Xiaobing Luo luoxb@hust.edu.cn School of Energy and Power Engineering, Huazhong University of Science and Technology, Wuhan 430074, People's Republic of China

study of the flow characteristics of ultrathin centrifugal fans is warranted.

Flow loss in turbomachinery can generally be classified into four main categories: profile loss, secondary loss, shock loss and leakage loss (Denton, 1993). In large scale turbomachinery, secondary loss is typically regarded as the primary contributor to overall flow losses due to the significant entropy generation caused by flow separation and mixing processes (Fan et al., 2022; Tang et al., 2022; Xu et al., 2023; Zheng et al., 2023). Additionally, leakage loss (Fristche et al., 2022) and shock loss (Guan et al., 2020) are also recognised as important factors. Flow separation is commonly observed on the suction side of blades, particularly at low flow rates (Jiang et al., 2022; Liu et al., 2022). In the case of ultrathin centrifugal fans, forward-curved blades are known for their ability to generate substantial static pressure increases. However, the adverse pressure gradient that develops within the blade passage often induces flow separation, leading to increased flow losses and a decrease in efficiency (Zhou et al., 2019). Despite the widespread use of forward-curved blades, most existing research has focussed on squirrel cage fans for ventilation, which typically feature a large hub ratio. For ultrathin centrifugal fans, a novel design has been developed that incorporates bionic blades inserted between adjacent blades to control flow separation. This innovative design has been shown to produce higher static pressure and reduce noise levels (Amer, 2023).

In addition to flow separation, boundary layer losses, also known as profile losses, are caused by viscous dissipation within the thin boundary layer. These losses are often overlooked due to their relatively small contribution to the total energy loss. However, in miniature centrifugal fans, the blade chord length plays a critical role in determining the pressure rise and airflow rate. Shorter blades can experience significant blockage of the flow passage due to the development of the boundary layer, leading to a more pronounced impact on fan performance (Walsh et al., 2010). In addition to the boundary layer on the blade surface, the boundary layer on the volute wall must also be considered. Since the ratio of the boundary layer thickness over the total axial height of the ultrathin centrifugal fan increases, the airflow rate may be significantly influenced. Moreover, this could lead to greater friction losses compared to those in large-scale turbomachinery. Modifications to the volute wall have been shown to effectively reduce noise and improve sound quality (Amer, 2024). In larger systems, the boundary layer on the volute surface is often overlooked due to the relatively large dimensions of the volute shell, and it has been suggested that friction on the volute wall can be neglected in double-suction centrifugal pumps (Deng et al., 2023). However, in ultrathin centrifugal fans, the impact of the volute wall boundary layer warrants detailed investigation.

Hence, the flow loss induced by flow separation is important but it remains a question whether the flow separation or boundary layer viscous dissipation is dominant in case of ultrathin centrifugal fans.

Apart from the flow loss mechanism in centrifugal fans, the turbulent characteristics are also worth investigating. The turbulent characteristics in a centrifugal fan considering the impeller-eccentric effect are carefully studied (Ren et al., 2022). The dipole source distributed on the pressure side of the squirrel cage fan blade is more intense than that on the suction side and this is due to the leading-edge vortices interacting with the pressure side of the blade. The vortex shedding due to flow separation is also distinct (Zaheer & Disimile, 2021). Tonal noise in a voluteless centrifugal fan is found to be due to the interaction between the inlet gap turbulence and rotating blades (Ottersten et al., 2021). The generation of low-frequency noise is experimentally verified to be caused by the flow separation and the blade profile should be designed with lower curvature to avoid flow separation (Fehse & Neise, 1999). The turbulence spectrum of the outflow plane is measured using Constant Temperature Anemometry and the results show that no inertial range with Kolmogorov's $-5/3$ power law can be detected, which indicates the turbulence is not fully developed and doesn't reach an equilibrium state (Hofer et al., 2021).

The noise generation mechanism is intrinsically transient and strongly related to its turbulent characteristics. Hence, the noise source in an ultrathin centrifugal fan needs deep investigation.

In this study, the Reynolds-Averaged Navier-Stokes (RANS) equations and Large Eddy Simulation (LES) are employed to investigate the flow characteristics and entropy production rates of an ultrathin centrifugal fan used in electronics cooling. The boundary layer is analyzed using both steady and transient simulations, with a particular focus on flow separation. This is explored through the application of the Q-criterion and wall shear stress analysis. Furthermore, entropy production is decomposed into terms related to molecular viscosity and eddy viscosity, allowing for a direct comparison of entropy production due to viscous dissipation within the boundary layer and flow separation at the blade tip. Additionally, hot-wire anemometry is utilised to obtain the turbulent energy spectrum, which is then compared with simulation results. Turbulence scales are examined to further characterise the turbulent flow field, while wall pressure fluctuations are analyzed in the frequency domain to identify potential noise sources. This study aims to

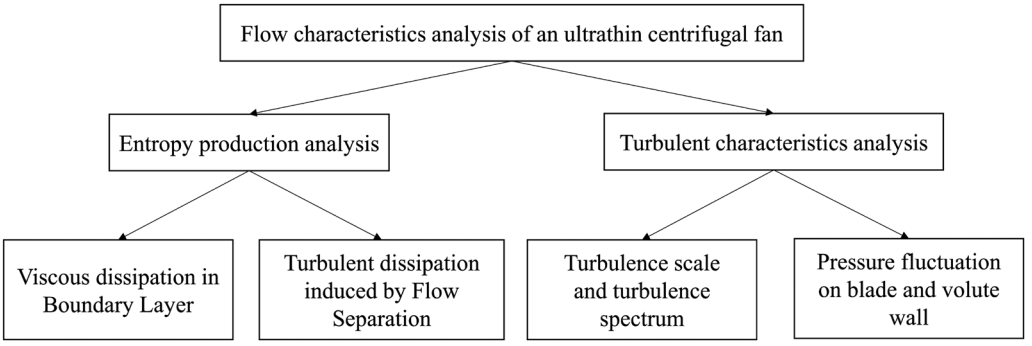

Figure 1. Flowchart of flow characteristics analysis of an ultrathin centrifugal fan.

Table 1. Structural parameters of the centrifugal fan.

Parameters	Magnitude
Vaneless diffuser outlet radius R_1 (mm)	39
Impeller blade outlet radius R_2 (mm)	24
Impeller blade inlet radius R_3 (mm)	12
Inlet diameter D_1 (mm)	38
Impeller outlet width W_1 (mm)	4
Impeller inlet width W_2 (mm)	3
Blade thickness T_1 (mm)	0.6
Blade inlet angle θ_1 (degree)	40.7
Blade outlet angle θ_2 (degree)	90
Volute width W_3 (mm)	8
Volute shell thickness T_2 (mm)	1.2
Opening angle θ_3 (degree)	107
Blade number N	47

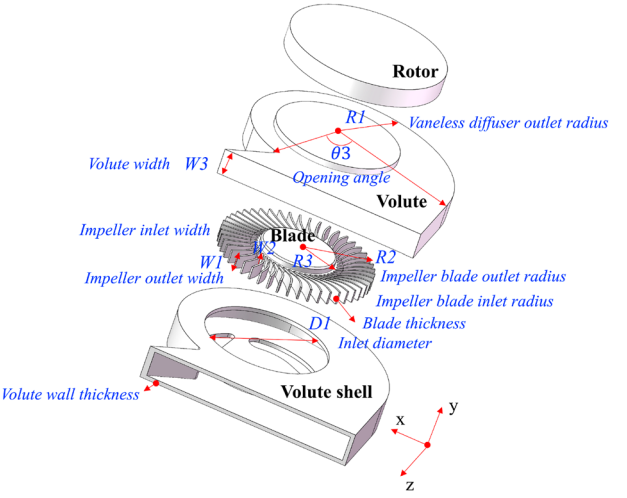

Figure 2. The structural model of the ultrathin centrifugal fan.

pinpoint the primary contributors to flow losses and elucidate the turbulence characteristics specific to the ultrathin centrifugal fan. Consequently, the findings not only offer valuable insights and specific recommendations for enhancing efficiency but also provide guidance on noise control strategies based on noise source localisation.

The research flowchart is presented in Figure 1 and the remaining part of this paper is organised as follows. Section 2 describes the structural parameters and operating parameters of the researched object. Section 3 details the adopted simulation method and Section 4 describes the numerical validation. Section 5 details the flow loss analysis and turbulent characteristics. The conclusion is drawn in Section 6.

2. Model description

The subject of this study, depicted in Figure 2, is an ultrathin centrifugal fan designed for forced cooling in laptops. The structural dimensions of the fan are provided in Table 1. Notably, the impeller lacks a ring at the blade tip, distinguishing it slightly from commercial fans. This modification was made to simplify the model, as the presence of the ring would introduce additional vortex shedding, which was not considered in this case.

The operation parameters are listed in Table 2. When the revolutionary speed is 5124 rpm, the centrifugal fan can generate an airflow of 3.7 g/s and a total pressure of 52.8 Pa. This is a simulation result and it has been validated to match well with the experimental results. The inlet and outlet are set to pressure outlet boundary condition and the gauge pressure is 0 Pa. The temperature is 20°C and the air density is 1.205 kg/m^3. The RF is 86.4 Hz and the BPF can be calculated by multiplying RF with the blade number.

3. Simulation and analysis method

RANS and LES are adopted to simulate the internal flow field of the centrifugal fan and ANSYS Fluent is used for simulation. The steady and transient features of the ultrathin centrifugal fan are studied. The inlet and outlet boundary conditions are set to ambient pressure conditions. The blade and volute wall are set as non-slip conditions. As the centrifugal fan is small the blade tip velocity is far smaller than sound velocity, the air is treated as incompressible.

Table 2. Operation parameters of the centrifugal fan.

Operating Parameters	Magnitude
Revolutionary speed (rpm)	5124
Flow rate (g/s)	3.7
Total pressure (Pa)	52.8
BPF (Hz)	4013.8
RF (Hz)	86.4

3.1. Simulation method

RANS eliminates the need to resolve most turbulence time and length scales. A closure for Reynolds stresses can fulfil the solution of the complete N-S equation based on the Boussinesq approximation, which relates the turbulent stress to the velocity gradient with turbulence viscosity (Sandberg & Michelassi, 2022).

Continuity equation for incompressible flow:

$$\frac{\partial v}{\partial x} = 0 \tag{1}$$

Momentum equation for incompressible and constant dynamic viscosity:

$$\rho \frac{\mathrm{d}u}{\mathrm{d}t} = -\frac{\partial P}{\partial x_i} + \mu \frac{\partial^2 u}{\partial x_j \partial x_j} + \rho f_i \tag{2}$$

In the steady simulation for the ultrathin centrifugal fan, the SST k-ω turbulence model is chosen due to its advantage for capturing flow separation, and the coupled pressure-velocity discretization scheme is chosen. The PRESTO! (PREssure STaggering Option) spatial discretization scheme is chosen for pressure as this discretization scheme is suitable for intense swirling flow. The rest of the variables' discretization scheme is chosen as second-order upwind for accuracy. The rotor region is set to frame motion to simulate the rotation effect of the blade. LES, different from the RANS, uses a subgrid model to simulate the subgrid stress (Tucker, 2011; Tucker, 2011). The filter, which normally is an implicit filter such as a grid filter, separates the simulated scale into the large scale that can be modelled directly and the subgrid scale that uses a subgrid model to simulate the subgrid stress. The filtered control equation is listed as follows: where τ_{ij} represents the subgrid stress. The bar on the variable represents the filtered value, the subgrid stress can be represented using Equation (4). There are many subgrid models to represent the subgrid stress, among which WALE (Wall-Adapting Local Eddy-viscosity) model shows its advantage in near-wall eddy-viscosity treatment (Kim et al., 2020). The mesh motion is set to simulate the rotation effect of the blade.

$$\frac{\partial \bar{u}}{\partial t} + \frac{\partial}{\partial x_j}(\bar{u}\bar{v}) = -\frac{1}{\rho}\frac{\partial \bar{P}}{\partial x_i} + \nu \frac{\partial^2 \bar{u}}{\partial x_j \partial x_j} - \frac{\partial \tau_{ij}}{\partial x_j} \tag{3}$$

$$\tau_{ij} = \overline{uv} - \bar{u}\bar{v} \tag{4}$$

In terms of LES, the setup needs to take more factors into consideration. Apart from the resolution, the discretization scheme option is of equal importance. The SIMPLEC (SIMPLE- Consistent) scheme is chosen and bounded central differencing is chosen for momentum discretization for less numerical dispersion and dissipation. The second-order implicit time advancement scheme is chosen for high accuracy. To make sure the flow is statistically steady, the data sampling starts until the blades rotate in 4 loops. In addition, to ensure the temporal and spatial resolution is adequate, the resolved turbulent kinetic energy should make up at least 80% of the total turbulent kinetic energy, and the Courant number should not be greater than 1 (Sorguven et al., 2022). This is a critical and rigorous simulation standard for LES, if not met, the simulation accuracy can't be guaranteed. Hence, the time-step is set as 1.63×10^{-5} s, which is exactly how long it takes for the impeller to rotate 0.5°.

3.2. Entropy production analysis method

The entropy production analysis method has been an intensely used tool for flow analysis because of its ability to quantify and locate the entropy production source. The entropy production theory is introduced and used to identify and quantify the flow loss in compressors (Denton & Pullan, 2012; Fan et al., 2022; Guan et al., 2020). Apart from that, by pinpointing the region where different kinds of flow loss occur and taking the integral of the entropy production rate over volume, the contribution of different kinds of flow loss such as shock loss, secondary loss, and boundary layer loss, are compared (Zhang et al., 2022). The entropy production method can also be used as an evaluation index for performance optimisation (Yadegari & Bak Khoshnevis, 2020; Zhang et al., 2022). In light of this, the entropy production analysis method is suitable for the flow loss analysis in the ultrathin centrifugal fan. However, in terms of separating different kinds of flow losses, it's quite an intractable challenge because different types of flow losses sometimes can be hard to distinguish from each other. Hence, using the inherent features of entropy production to differentiate the flow loss is a wise method.

Entropy production is induced by irreversible processes like secondary flow, flow separation, and viscosity-induced turbulent dissipation. The entropy production analysis method can help locate where the flow loss is the most significant and better understand the loss mechanism in the centrifugal fan. Their expressions are listed

as follows:

$$\rho\frac{DS}{Dt}=\frac{\Phi+\Phi_T}{T}+\frac{\gamma}{T^2}(\nabla T)^2 \tag{5}$$

$$\Phi=\tau_{ij}\frac{\partial u}{\partial x_j} \tag{6}$$

$$\Phi_T=-\rho\overline{uv}\frac{\partial\bar{v}}{\partial x_j}=\frac{\mu_t}{\mu}\overline{\tau_{ij}}\frac{\partial\bar{v}}{\partial x_j} \tag{7}$$

where Φ represents the viscous dissipation induced entropy production terms, Φ_T represents the turbulent entropy production terms.

Normally, the entropy production terms are divided into time-averaged terms (Equation 8) and fluctuating terms (Equation 9) (Xu et al., 2024; Zhou et al., 2022), and the fluctuating terms is calculated by multiplying the viscosity induced strain and the gradient of the fluctuating velocity (Herwig & Kock, 2006; Kock & Herwig, 2004, 2005),

$$\begin{aligned}S_{\text{mean}}=\frac{\mu_{\text{eff}}}{T}\Bigg\{&2\left[\left(\frac{\partial\bar{u}}{\partial x}\right)^2+\left(\frac{\partial\bar{v}}{\partial y}\right)^2+\left(\frac{\partial\bar{w}}{\partial z}\right)^2\right]\\&+\left(\frac{\partial\bar{u}}{\partial y}+\frac{\partial\bar{v}}{\partial x}\right)^2+\left(\frac{\partial\bar{u}}{\partial z}+\frac{\partial\bar{w}}{\partial x}\right)^2\\&+\left(\frac{\partial\bar{v}}{\partial z}+\frac{\partial\bar{w}}{\partial y}\right)^2\Bigg\}\end{aligned} \tag{8}$$

$$\begin{aligned}S_{\text{tur}}=\frac{\mu_{\text{eff}}}{T}\Bigg\{&2\left[\left(\frac{\partial u'}{\partial x}\right)^2+\left(\frac{\partial v'}{\partial y}\right)^2+\left(\frac{\partial w'}{\partial z}\right)^2\right]\\&+\left(\frac{\partial u'}{\partial y}+\frac{\partial v'}{\partial x}\right)^2+\left(\frac{\partial u'}{\partial z}+\frac{\partial w'}{\partial x}\right)^2\\&+\left(\frac{\partial v'}{\partial z}+\frac{\partial w'}{\partial y}\right)^2\Bigg\}\end{aligned} \tag{9}$$

where μ_{eff} represents the effective viscosity of air and is the sum of the viscosity and eddy viscosity as shown in Equation (10), and u, v, w represents the three components of velocity on three orthogonal directions,

$$\mu_{eff}=\mu+\mu_t \tag{10}$$

In RANS simulation, the fluctuating terms can't be calculated directly, so the turbulent dissipation rate ϵ is introduced to calculate the fluctuating terms of the entropy production.

$$S_{tur}=\frac{\rho\epsilon}{T} \tag{11}$$

LES and RANS method are conducted simultaneously to investigate the entropy production on the turbomachines, the results indicating the fluctuating terms are nonnegligible and LES is advantageous to RANS in capturing fluctuating terms (Borcherding et al., 2023; Marconcini et al., 2019; Zhao & Sandberg, 2020). Hence, it's necessary to adopt LES to accurately explore the flow loss characteristics of the ultrathin centrifugal fan.

In this work, to separate the entropy production induced by the boundary layer and flow separation, the entropy production is divided into viscosity terms and eddy viscosity terms. As the boundary layer is where viscosity dominates, the entropy production in the boundary layer can be calculated directly by taking the integral of Equation (12) over the whole volume. In addition, the flow separation normally occurs in flow passage between adjacent blades and this is where eddy viscosity dominates. Hence, the entropy production induced by flow separation can be calculated by taking the integral of Equation (13) over the whole volume. By utilising the intrinsic features of viscosity, there's no need to bother to locate the different areas where different physical process occurs. Moreover, this assumption has been validated through the simulation that the entropy generated by the mean flow effects concentrates in the blade boundary layer, while the turbulence-induced entropy is distributed in the wake region with vortex shedding (Zhao & Sandberg, 2020).

$$\begin{aligned}S_{\text{vis}}=\frac{\mu}{T}\Bigg\{&2\left[\left(\frac{\partial\bar{u}}{\partial x}\right)^2+\left(\frac{\partial\bar{v}}{\partial y}\right)^2+\left(\frac{\partial\bar{w}}{\partial z}\right)^2\right]\\&+\left(\frac{\partial\bar{u}}{\partial y}+\frac{\partial\bar{v}}{\partial x}\right)^2+\left(\frac{\partial\bar{u}}{\partial z}+\frac{\partial\bar{w}}{\partial x}\right)^2\\&+\left(\frac{\partial\bar{v}}{\partial z}+\frac{\partial\bar{w}}{\partial y}\right)^2\\&+2\left[\left(\frac{\partial u'}{\partial x}\right)^2+\left(\frac{\partial v'}{\partial y}\right)^2+\left(\frac{\partial w'}{\partial z}\right)^2\right]\\&+\left(\frac{\partial u'}{\partial y}+\frac{\partial v'}{\partial x}\right)^2+\left(\frac{\partial u'}{\partial z}+\frac{\partial w'}{\partial x}\right)^2\\&+\left(\frac{\partial v'}{\partial z}+\frac{\partial w'}{\partial y}\right)^2\Bigg\}\end{aligned} \tag{12}$$

$$\begin{aligned}S_{\text{eddy\_vis}}=\frac{\mu_t}{T}\Bigg\{&2\left[\left(\frac{\partial\bar{u}}{\partial x}\right)^2+\left(\frac{\partial\bar{v}}{\partial y}\right)^2+\left(\frac{\partial\bar{w}}{\partial z}\right)^2\right]\\&+\left(\frac{\partial\bar{u}}{\partial y}+\frac{\partial\bar{v}}{\partial x}\right)^2+\left(\frac{\partial\bar{u}}{\partial z}+\frac{\partial\bar{w}}{\partial x}\right)^2\\&+\left(\frac{\partial\bar{v}}{\partial z}+\frac{\partial\bar{w}}{\partial y}\right)^2\\&+2\left[\left(\frac{\partial u'}{\partial x}\right)^2+\left(\frac{\partial v'}{\partial y}\right)^2+\left(\frac{\partial w'}{\partial z}\right)^2\right]\end{aligned}$$

$$+\left(\frac{\partial u'}{\partial y}+\frac{\partial v'}{\partial x}\right)^2+\left(\frac{\partial u'}{\partial z}+\frac{\partial w'}{\partial x}\right)^2 +\left(\frac{\partial v'}{\partial z}+\frac{\partial w'}{\partial y}\right)^2\Bigg\} \tag{13}$$

Hence, calculating the entropy production associated with viscosity throughout the entire centrifugal fan makes it possible to directly compare the entropy production caused by flow separation or boundary layer effects. This information can be used to pinpoint areas for improving the operating efficiency of the ultra-thin centrifugal fan.

3.3. Turbulence scale and transient analysis method

The turbulence timescale is determined by calculating the self-correlation of the velocity time series. It is crucial to exclude the periodic fluctuation of the flow field to accurately calculate the turbulence timescale. Auto-corelation is a two-point correlation in time (He et al., 2002; Nguyen et al., 2021):

$$B_{11}(t_A,\hat{t}) = \overline{u'(t_A)u'(t_A+\hat{t})} \tag{14}$$

The normalised auto-correlation reads:

$$B_{11}^{\text{norm}}(\hat{t}) = \frac{\overline{u'(t_A)u'(t_A+\hat{t})}}{u_{\text{rms}}^2} \tag{15}$$

where $v_{1,rms}$ represents the root mean square of the velocity.

Taking integral on the normalised auto-correlation can get integral timescale:

$$T_{\text{int}} = \int_0^\infty B_{11}^{\text{norm}}(\hat{t})\,\mathrm{d}\hat{t} \tag{16}$$

As the temporal auto-correlation is much easier to measure than the two-point correlation, Taylor's hypothesis of frozen turbulence is introduced here to calculate the length scale.

$$L_{\text{int}} = v_{\text{mean}} \cdot T_{\text{int}} \tag{17}$$

Apart from the turbulence scale analysis, the turbulent energy spectrum is calculated to explore the characteristics of turbulent kinetic energy transfer. In the hot-wire anemometer measurement, the sampling time interval is 0.00005 s and the calculated maximum frequency reaches 10,000 Hz based on the Nyquist sampling principle. The sampling duration time is 2.5 s so the frequency resolution is 0.4 Hz and there is a total amount of 50000 sampling points. To get the turbulent energy spectrum, the windows function is set to box window and the overlapping ratio is 50%. The Welch's method is used to compute the Power Spectral Density (PSD). Along with exploring the turbulent energy spectrum, it's worthwhile to examine the Rotation Frequency (RF) and Blade Passing Frequency (BPF) as well as their higher harmonics component of the static pressure fluctuation on the wall. This fluctuation is also a sound source, and studying the frequency components can aid in pinpointing the source of the sound and comparing surface contributions between the blade and volute wall.

4. Numerical validation

4.1. Spatial and temporal resolution evaluation

The spatial and temporal resolution is essential to get accurate simulation results. First, the boundary layer resolution should be adequate for LES. The nondimensional first grid height y^+ should be below 1. The y^+ contour shown in Figure 3(a,b) shows that the height of the first grid in the boundary layer is reasonable. To accurately capture the velocity gradient of the boundary layer, there are 10 layers of boundary layer gird and the inflation ratio is set to 1.1 and the transition from the boundary layer grid to the volumetric grid is smooth. All the solid walls are covered with boundary layer grids to capture the flow separation.

In LES, the turbulent kinetic energy consists of two parts, most of which should be resolved by the grid, the rest of the energy is referred to as subgrid turbulent kinetic energy which can't be directly calculated. The spatial resolution of the grid is evaluated by the ratio of resolved turbulent kinetic energy to the total turbulent kinetic energy as shown in Equation (18). This ratio should exceed 80%, indicating the grid can resolve most of the turbulent kinetic energy and the simulation accuracy can be guaranteed.

$$R_{\text{spa}} = \frac{k_{\text{res}}}{k_{\text{res}}+k_{\text{sgs}}} \tag{18}$$

To meet the resolution standard of the spatial resolution, the mesh we adopt consists of 21.2 million tetrahedral grids, among which there are 13.6 million grids in the volute region and 7.6 million grids in the rotor region. The local magnification diagram of the mesh near the volute tongue is presented in Figure 3(e). From Figure 3(c), the spatial resolution in the middle cutting plane shows that the resolution is beyond 0.8 in all areas. This demonstrates the spatial resolution of this mesh is satisfying.

It is important to consider both spatial and temporal resolution, with the latter being evaluated by the Courant number. This dimensionless parameter indicates the ratio of the distance travelled by the working

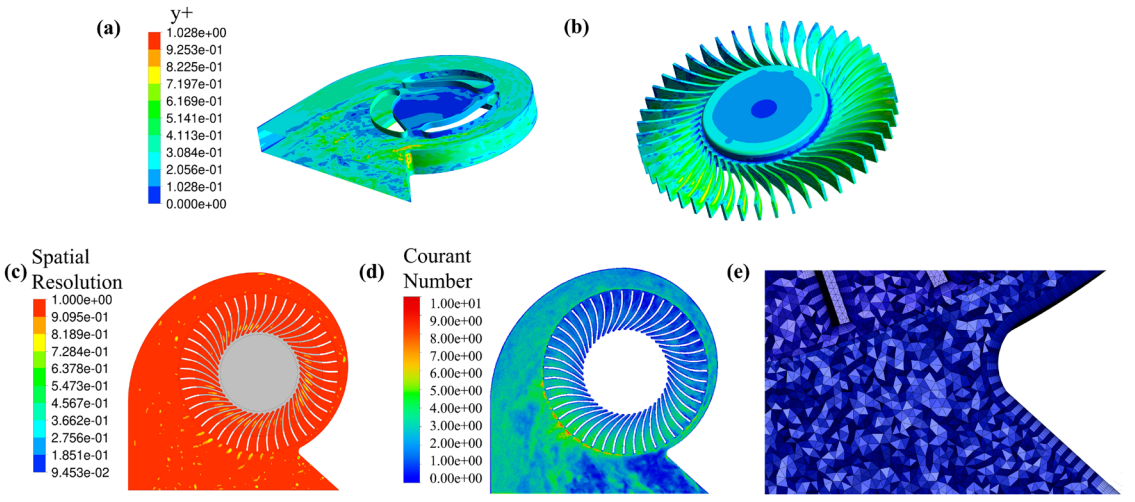

Figure 3. (a) y plus on the volute wall (b) y plus on the blade surface (c) Spatial resolution on the mid-cutting plane (d) Courant number on the mid-cutting plane (e) Local magnification diagram of the grid near the volute tongue.

medium during a single time step to the size of the grid. Ideally, the Courant number should be as close to 1 as possible. Based on Figure 3(d), the Courant number ranges from 3 to 5 in most areas, except for a large Courant number area near the edge of the impeller. Taking into account the balance between computational resources and accuracy, the chosen time step is deemed satisfactory.

4.2. Hot-wire measurement and simulation comparison

Turbulence velocity spectra are usually used to validate the numerical accuracy of the simulation (Grace, 2015; Lewis et al., 2023). To validate that the spatial and temporal resolution is adequate, four points out of a sampling line are picked up to compare the turbulent energy spectrum between the simulation and experimental results (depicted in Figure 4). The probe is inserted into the flow field and the direction is parallel with the flow direction. The spacing between the four points is 12 mm.

Figure 5 illustrates the comparison, where the red solid line represents the simulation results and the black solid line represents the experimental results. The turbulent energy spectrum of the simulation and experimental results match well at points 2 and 3, which are in the middle range of the outlet shown in Figure 4. However, at point 1, located far from the volute tongue, the simulation turbulent energy spectrum deviates from the experimental turbulent energy spectrum in the high-frequency range. Meanwhile, at point 4, near the volute tongue, the simulation turbulent energy spectrum amplitude is smaller than that of the experimental results overall. There are several reasons for the deviation. Firstly,

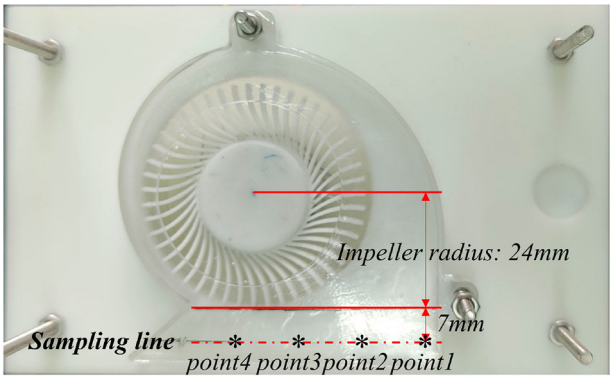

Figure 4. Hot-wire anemometer measurement setup and four sampling points for comparison between simulation and experimental results.

due to limitations in computational resources, the simulation sampling accuracy can't match that of the hot-wire measurement, resulting in some characteristic frequencies disappearing in the simulation spectra. Secondly, the aliasing of the data can be a source of error because the hot-wire anemometer systems utilise low-pass filters with corner frequencies equal to or larger than 10 kHz.

In conclusion, the simulation accuracy is validated through experimental validation. In the following section, the internal flow characteristics of the ultrathin centrifugal fan are analysed.

5. Results and discussion

5.1. Flow characteristics analysis

5.1.1. Boundary layer effect

Ultrathin centrifugal fan, unlike large turbomachinery for industrial ventilation, is designed for small and

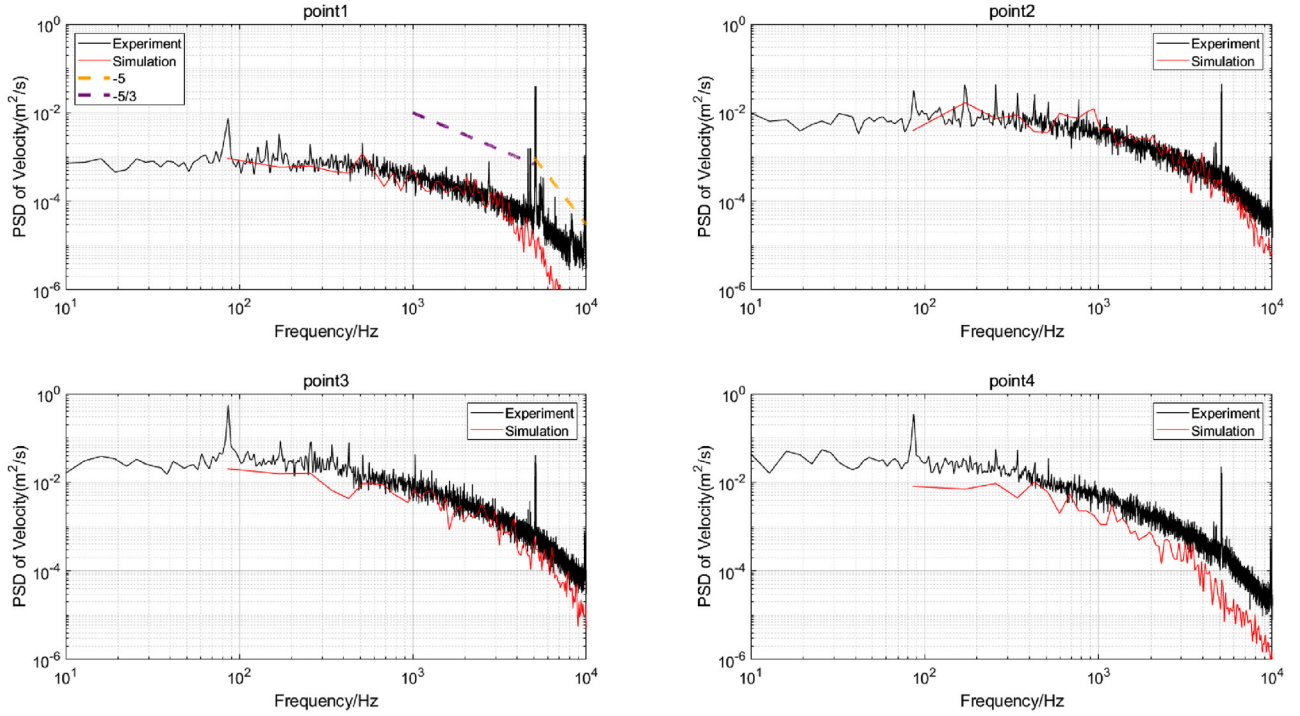

Figure 5. Turbulent energy spectrum comparison between the experiment and simulation results.

confined spaces. Hence, the axial dimension is very small and the boundary layer thickness is inevitably nonnegligible. It's bound to have some negative effect on the overall mass flow rate. This blockage needs to be quantified and its steady and transient characteristics are both investigated. Figure 6 depicts the steady characteristics of the velocity profile calculated by RANS. Six monitoring lines have been established to analyse the characteristics of the boundary layer. As depicted in Figure 6(a), two of these lines which are perpendicular to the rotation axis are located near the fan outlet. They are used to examine the relationship between non-dimensional velocity and y+. The remaining four lines are parallel to the rotation axis and are used to measure the total thickness of the volute from its upper to lower wall. As shown in Figure 6(b), the buffer layer, which typically ranges from 5 to 30 in flow over a flat plate, doesn't have a distinct boundary. This may be due to the high Reynolds number of the flow. Due to the significant inertial effect, the shear flow is prone to detach rapidly from wall effects and directly into the logarithmic layer. However, the logarithmic layer ranges from 5 to 20 in Line 1 and Line 2 and the non-dimensional velocity curve remains turbulent until y+ reaches 20. This further confirms that the flow in the ultrathin centrifugal fan is highly turbulent.

The velocity profiles of Lines 3 through 6 are arranged in a radial pattern around the impeller, with each line separated by 90°. Line 6 is positioned at the volute tongue. From Figure 6(c), Lines 3 and 4 have the flattest velocity profiles, while Line 5 displays strong asymmetry on both ends due to the blade's axial direction asymmetry. The weirdest velocity profile occurs in Line 6, which reaches its peak velocity near the hub plane. The boundary layer thickness is approximately 0.4 mm on both the upper and lower walls of the volute, with a total thickness accounting for around 10% of the volute's height. This proportion is significant compared to a large centrifugal fan, indicating that the boundary layer effect cannot be ignored in ultrathin centrifugal fans. Additionally, its transient characteristics are also worth investigating.

Figure 7 depicts the transient characteristics of the boundary layer. A total amount of 50 points is sampled to monitor the velocity fluctuation of one line in one flow period. The monitoring lines are depicted in Figure 7(a). As shown in Figure 7(d), the irregular inlet consists of 3 strip-like inlets because of the installation of a motor. They are at the plane of $y = 8$ mm and the regular inlet is circular which is located at the plane of $y = 0$ mm. The mean velocity profile with an error bar representing the velocity fluctuation is depicted in Figure 7(b,c,e,f).

From Figure 7(b,e), it's clear that the velocity near the irregular inlet fluctuates more intensely than the regular inlet in Lines 1,2,3, and Line 7, among which Line 7 set in the outlet region fluctuates most intensely. This could be due to the irregular configuration leading to more turbulent inlet conditions. Moreover, the blade width is growing from hub to tip so the flow can be fully developed when it gets to the blade tip. In addition, the fluctuation

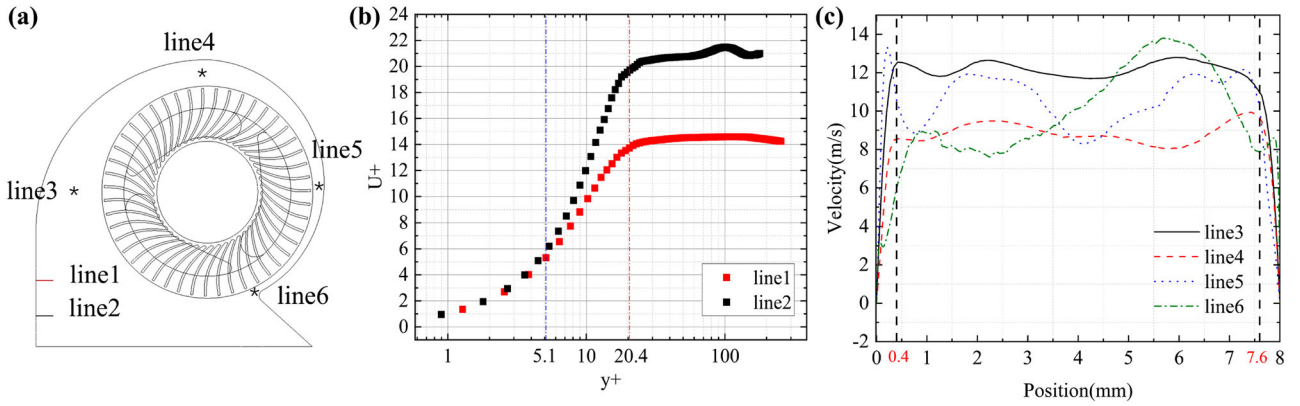

Figure 6. (a) Monitoring lines position for steady simulation (b) The dimensionless velocity relation with the y+ in Line 1 and Line 2 (c) The velocity profile in Lines 3,4,5 and 6.

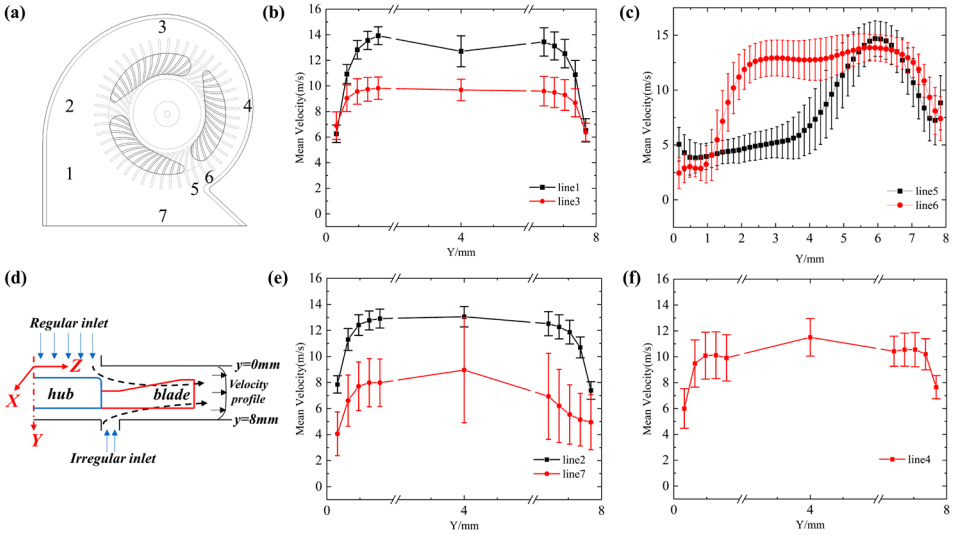

Figure 7. (a) Monitoring lines position for transient simulation (b) Velocity profiles in Line 1,3 (c) Velocity profiles in Line 5 and Line 6 near volute tongue (d) The cross-section schematic of the ultrathin centrifugal fan (e) Velocity profiles in Line 2,7 (f) Velocity profiles in Line 4.

gets more intense when the monitoring point is closer to the core region. This is mainly due to the constraining effect of the wall. There is also an exception in that the fluctuation in Line 4 shown in Figure 7(f) shows the opposite pattern compared to the other lines.

As depicted in Figure 7(c), Line 5 and Line 6 are two monitoring lines positioned near the volute tongue. Line 5 is placed outside the flow passage, whereas Line 6 is located within it. The velocity profiles of the two lines exhibit distinctive characteristics, with Line 6 presenting asymmetry on both ends of the wall and Line 5 outside the flow passage showing a peak velocity. The velocity profile of Line 5 is heavily influenced by the flow in the blade passage due to its proximity to the blade outlet, indicating non-uniform flow in the blade passage on the axial dimension. On the other hand, the backflow affects the velocity profile of Line 6, causing a bump in the midrange velocity profile while still displaying significant blockage. Since the volute tongue is the critical area limiting the flow rate of the fan, it is crucial to carefully design the match between the impeller and the volute.

5.1.2. Flow separation

Flow separation in an ultrathin centrifugal fan will harm the operation efficiency because the mixing of secondary flow induces irreversible entropy production. The *Q*-criterion method and wall shear stress analysis method are introduced to analyse the flow separation effect.

Figure 8 illustrates the vortex distribution on four cutting planes and their heights are 3 mm, 4 mm, 5 mm, and 5.8 mm respectively. As shown in Figure 8, it's distinct that the vortex distribution isn't uniform in the circumferential direction. The blade passages near the outlet present a larger *Q* magnitude than the inner blade passage, which should be attributed to the asymmetric structure of the volute shell.

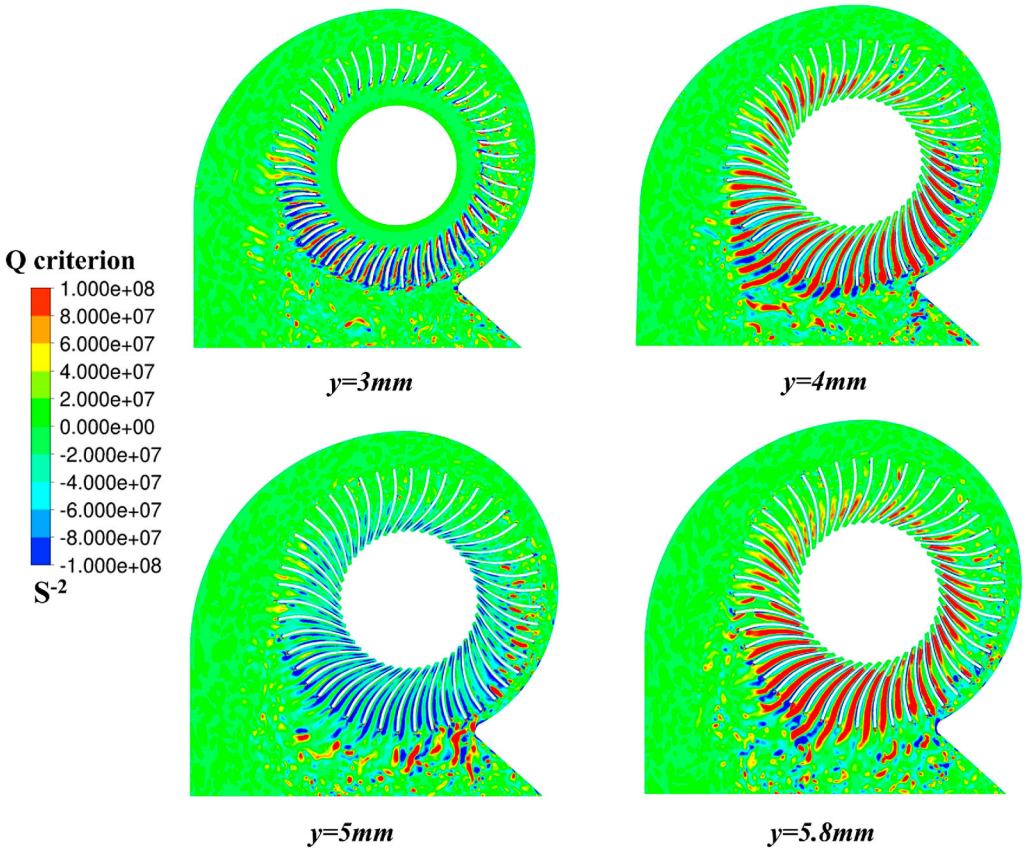

Figure 8. Q criterion at cutting planes of different heights.

In terms of the difference in the axial dimension, the Q contour at the four cutting planes should be carefully observed. At the cutting plane of $y = 3$ mm which is near the shroud of the blade so that the blade is cut partly, the flow separation starts at the root of the blade. There are two distinct regions featuring positive Q magnitude and negative Q magnitude. Regions of positive Q are where vorticity dominates while regions of negative Q are where viscous stress dominates. The positive Q magnitude is mainly in the flow passage and negative Q magnitude is mainly near the blade surface.

Contra-rotating vortex exists in one flow path. At the cutting plane of $y = 4$ mm, the vortex distribution is different, the positive Q magnitude region is filled in the flow passage near the outlet and undoubtedly vortex is blocking the natural flow, inducing flow loss. When the cutting plane moves further to the hub of the impeller, the Q magnitude suddenly decreases at the cutting plane of $y = 5$ mm indicating the vorticity is not strong at this plane. It can be deduced that the vortex core region isn't larger than 1 mm. At the lowest cutting plane near the hub, the vortex magnitude goes up and the distribution pattern becomes similar to that at the cutting plane of $y = 4$ mm. In conclusion, the vortex distribution is not homogeneous in the axial direction and there exist two vortex core regions, and the vortex is limited to two adjacent blades and formed into a strip. Two cores are distributed in one flow passage. According to the contour of the Q criterion, the vortex is blocked in the flow passage of two adjacent blades and the vortex is extended with the blade wake all along to the volute region, mixing with the less turbulent flow. And between two positive regions marked in red lies a negative region core marked in blue, indicating that a strong turbulent mixing process happens in the outlet of two adjacent blades. Through further observation, the suction side of the blade is where flow separation happens. The vortex strip stems from the root of the blade and extends to the middle region between the two blades.

Figure 9 depicts the distribution of wall shear stress on the blade and volute surface. Figure 9(a) shows two small areas of low magnitude distributed on the hub and shroud of the blade on the suction side. The distribution pattern is different on the pressure side, indicating flow separation in the middle region of the pressure side and at both ends on the suction side. Comparing Figures 9(a) and 8, it is evident that the flow separation is nonuniform in the axial dimension. Flow separation mainly occurs in the middle range of the pressure side, caused by the mismatch between the airflow inlet angle and the blade inlet mounting angle. Additionally, flow separation also

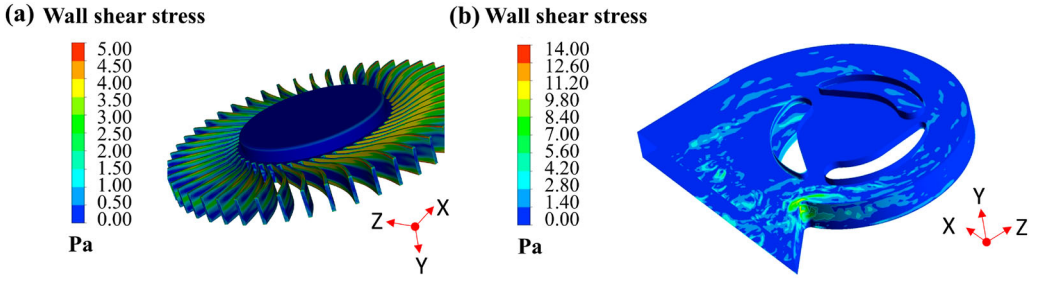

Figure 9. (a) Wall shear stress contour on blade surface (b) Wall shear stress contour on volute wall surface.

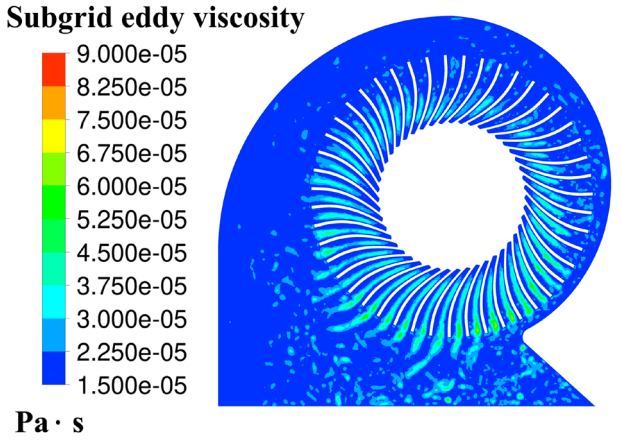

Figure 10. Subgrid eddy viscosity distribution.

occurs at the hub and shroud of the suction side due to a large adverse pressure gradient. In addition, Figure 9(b) shows the wall shear stress on the volute wall. The highest wall shear stress is concentrated on the volute tongue area, surpassing that on the blade surface. This is likely due to the periodic flush out of the rotating blades. It indicates that the volute tongue region experiences viscous dissipation, and entropy production related to viscosity dominates in this area. The following section will provide further analysis to confirm this point.

5.1.3. Entropy production rate comparison

Flow separation and viscous dissipation are always accompanied by entropy production, from which researchers can easily characterise the flow loss location and magnitude. As mentioned before, the viscosity dissipation mainly occurs in the boundary layer, and eddy viscosity is associated with turbulent flow, such as flow separation. In addition, the eddy-viscosity should vanish in the boundary layer so that the assumption would make sense. The eddy viscosity distribution is shown in Figure 10. It can be seen that the eddy-viscosity is mainly distributed in the blade passage and it vanishes near the wall boundary. The interlink between the viscosity, eddy viscosity, and their related entropy production needs further validation.

The entropy production can be divided into four terms, viscosity-induced time-averaged terms, viscosity-induced fluctuating terms, eddy viscosity-induced time-averaged terms, and eddy viscosity-induced fluctuating terms. The different terms of entropy production are illustrated in Figures 11(a–c), and 11(d) in turn. These figures are obtained by volume rendering and the transparency is set to 20% so the distribution of entropy production rate can be seen. From Figure 11(a,b), the viscosity-induced entropy production is mainly distributed in the boundary layer. The fluctuating terms mainly concentrate on the outlet region in the hub plane due to the intense turbulence here, which is confirmed in the boundary layer transient analysis. From Figure 11(c,d), there is a distinct difference in that the eddy viscosity-induced time-averaged terms are distributed more widely than the eddy viscosity-induced fluctuating terms. They mainly concentrate on the rotor region and the maximum area coincides well with the region where flow separation occurs.

By superimposing Figures 11(a,b,e) is obtained, featuring the distribution of entropy production induced by viscosity. Similarly, Figure 11(f) is obtained from the same process and displays the distribution of entropy production induced by eddy viscosity. A clear difference emerges when comparing these two types of viscosity-induced entropy productions. Viscosity terms tend to concentrate on the boundary layer, while eddy viscosity terms concentrate on the rotor region and its outer extended region. Furthermore, the maximum viscosity-induced entropy production reaches 10 W/K and is distributed more widely than the eddy viscosity-induced entropy production. From this, we can conclude that viscosity-induced entropy production dominates in the ultrathin centrifugal fan. To get further quantified comparison, it is necessary to perform a volume integral over different terms.

The integral results are shown in Table 3. Undoubtedly, the viscosity-induced time-averaged terms' volume integral over the volute region produces the largest entropy production, reaching 1.52×10^{-4} W/K. In addition, the eddy viscosity-induced entropy production

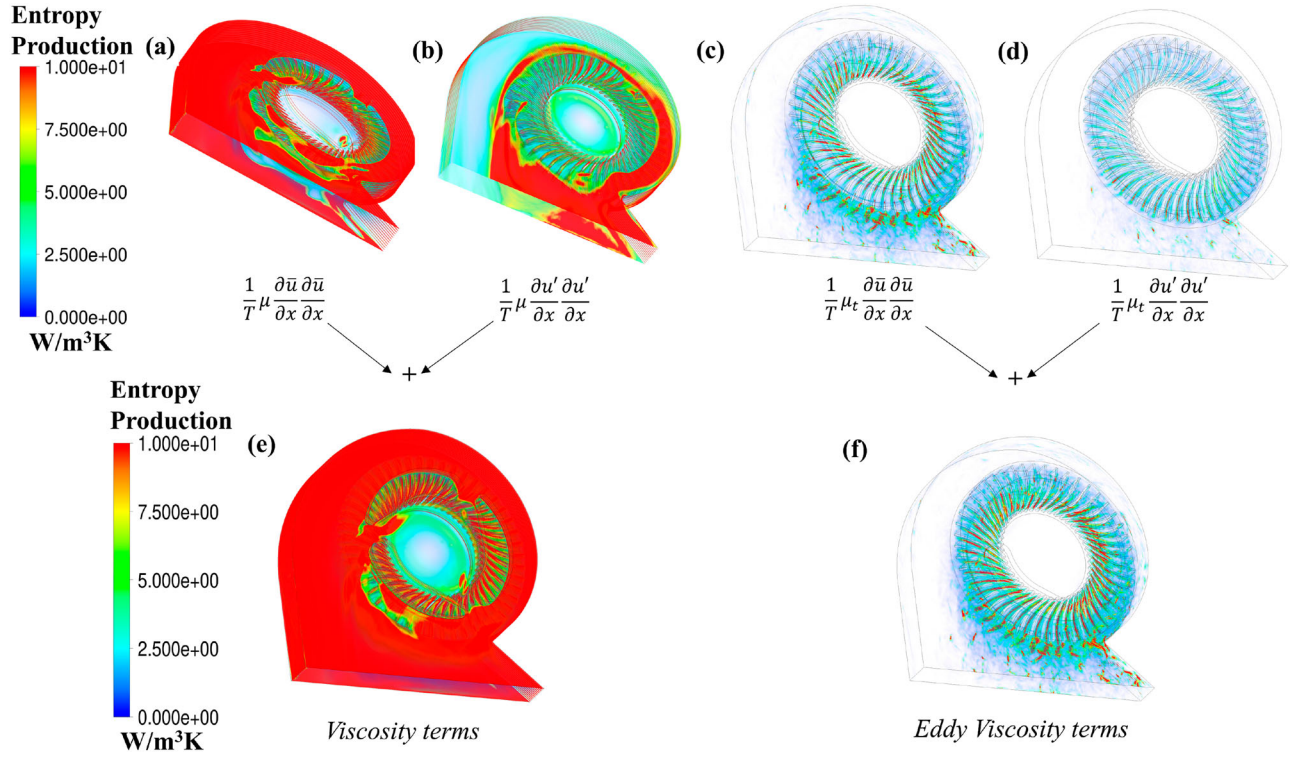

Figure 11. (a) Volume rendering of the viscosity-induced time-averaged entropy production (b) Volume rendering of the viscosity-induced fluctuating entropy production (c) Volume rendering of the eddy viscosity-induced time-averaged entropy production (d) Volume rendering of the eddy viscosity-induced fluctuating entropy production (e) Volume rendering of the viscosity-induced entropy production (f) Volume rendering of the eddy viscosity-induced entropy production.

Table 3. Entropy production rate integral on rotor region and volute region.

	Rotor (W/K)	Volute (W/K)	Sum (W/K)
Viscosity-induced time-averaged terms	5.35×10^{-5}	1.52×10^{-4}	2.75×10^{-4}
Viscosity-induced fluctuating terms	4.87×10^{-5}	2.09×10^{-5}	
Eddy viscosity induced time-averaged terms	4.73×10^{-6}	3.72×10^{-6}	1.16×10^{-5}
Eddy viscosity induced fluctuating terms	3.05×10^{-6}	5.01×10^{-7}	
Sum (W/K)	1.1×10^{-4}	1.77×10^{-4}	2.87×10^{-4}

has an order of magnitude difference compared with the viscosity-induced entropy production, which is also reflected evidently in Figure 10. The sum of the viscosity-induced entropy production reaches 2.75×10^{-4} W/K, while the eddy viscosity-induced entropy production is only 1.16×10^{-5} W/K, making up 4.1% of the total entropy production. This fact demonstrates that the entropy production in the boundary layer is the main contributor to the flow loss. The flow separation-induced flow loss, although apparent in the ultrathin centrifugal fan, can be neglected when compared with the boundary layer loss.

In terms of the entropy production rate in rotor and volute region, the difference isn't so distinct. The entropy production rate in volute region is 1.77×10^{-4} W/K while the entropy production rate in rotor region is 1.1×10^{-4} W/K. It's evident that the volute region experiences the majority of flow loss. This is due to the dominant viscous dissipation in the boundary layer of the upper and lower volute face. In the case of the ultrathin centrifugal fan, the boundary layer effect is intensified by the reduced axial dimension. As a result, the flow loss in the boundary layer becomes the primary concern for designers aiming to enhance the efficiency of the ultrathin centrifugal fan.

5.2. Turbulent characteristics analysis

5.2.1. Turbulence scale

In Figure 12, turbulent characteristics of the ultrathin centrifugal fan are presented. The distribution of the RMSE velocity is depicted in Figure 12(a). The flow passage exhibits the highest turbulent intensity, and the outlet region also shows a distinct area of high RMSE velocity. In this zone, there are 25 monitoring points spaced 2 mm apart, utilised to assess the turbulent characteristics using a hot-wire anemometer. The measurement results, including timescale and RMSE velocity, are plotted against the monitoring point position in Figure 12(b). The simulation results display a slightly

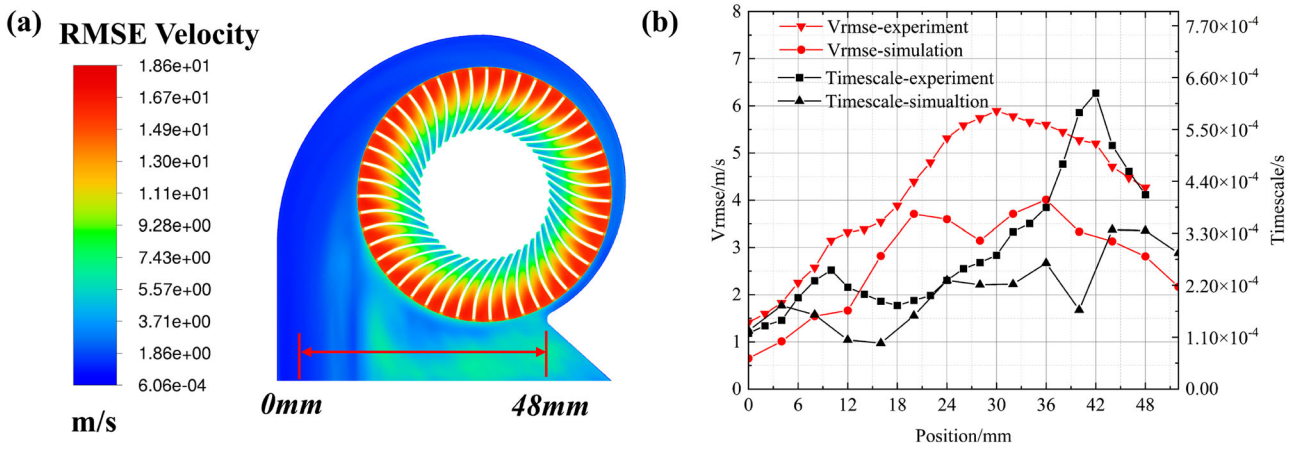

Figure 12. (a) RMSE velocity contour at $y = 4$ mm and a general view of motoring line for hot-wire anemometer measurement (b) The experimental and simulation result of hot-wire anemometer test at monitoring line

smaller amplitude than the experimental results, demonstrating a similar trend. The deviation between the experiment and simulation results increases as the monitoring point nears the volute tongue. This disparity can be attributed to the longer sampling time of the experiment, enabling the capture of more turbulent information.

From the comparison of the trend of timescale and RMSE velocity, we can find they demonstrate different tendencies. RMSE velocity reaches its maximum in the middle range of the monitoring line. It's consistent with the trend shown in Figure 12(a), which corresponds to the blade wake area. However, the trend of the timescale reaches its maximum near the volute tongue at position $= 42\ mm$. This indicates that the turbulence time scale is large here and it takes a relatively long time for a coherent structure to cross inertial range to dissipation range. Considering Taylor's frozen hypothesis, the length scale of the coherent structure is relatively large here. It can be deduced that the volute tongue area is where the low-frequency noise source is located.

Figure 13 presents a comparison between experimental and simulation results for the turbulent energy spectrum, demonstrating a good overall agreement. However, the simulation spectrum exhibits a lower frequency resolution, which limits its ability to capture the rotational frequency (RF) and its higher harmonic components as observed in the experimental spectrum. The turbulent energy spectrum adheres to the Kolmogorov −5/3 power law within the 1000 Hz to 5000 Hz frequency range, indicating that the turbulence is fully developed and has reached an equilibrium state. In the higher frequency range of 5000 Hz to 10,000 Hz, the spectrum follows a −5 power law, suggesting a more intense turbulent cascade, where smaller eddies exhibit a greater rate of turbulent energy transfer.

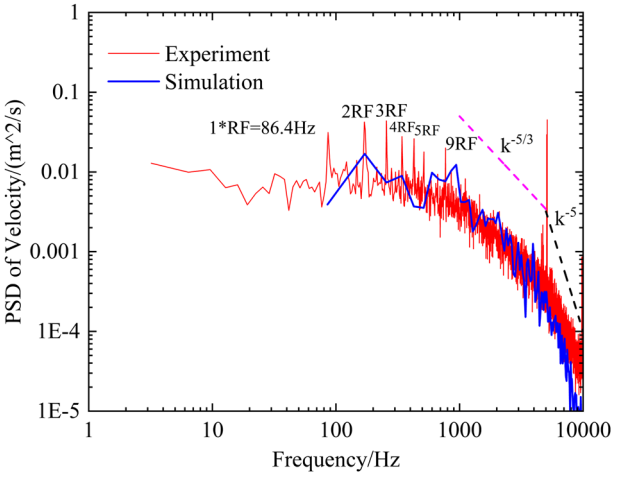

Figure 13. Turbulent kinetic energy spectrum comparison between the experimental and simulation results.

5.2.2. *Pressure fluctuation on surface*

Figure 14 illustrates the RMS pressure fluctuation on the surface of the volute and blade. The legend bar shows that the maximal pressure fluctuation reaches 55 Pa on the blade surface, which is located on the blade tip area of the pressure side. The blade tip of the suction side is where the flow separation occurs and this point can be validated from the wall shear stress distribution. On the volute wall, the maximal pressure fluctuation is 45 Pa, distributed on the area where the volute tongue is central. The distribution of the RMS pressure fluctuation reflects that the turbulence intensity is high there and the area is where the dipole source is located. However, the RMS pressure fluctuation distribution is demonstrated as a whole so the frequency components can't be distinguished from the contour. Hence, the pressure fluctuation related to some focussed frequency components such as BPF and RF and its higher harmonics should be emphatically studied.

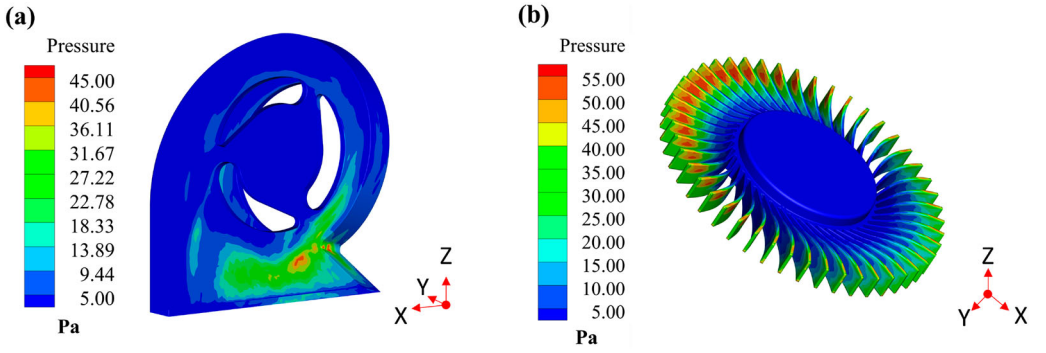

Figure 14. (a) RMS pressure fluctuation on the volute wall (b) RMS pressure fluctuation on the blade surface.

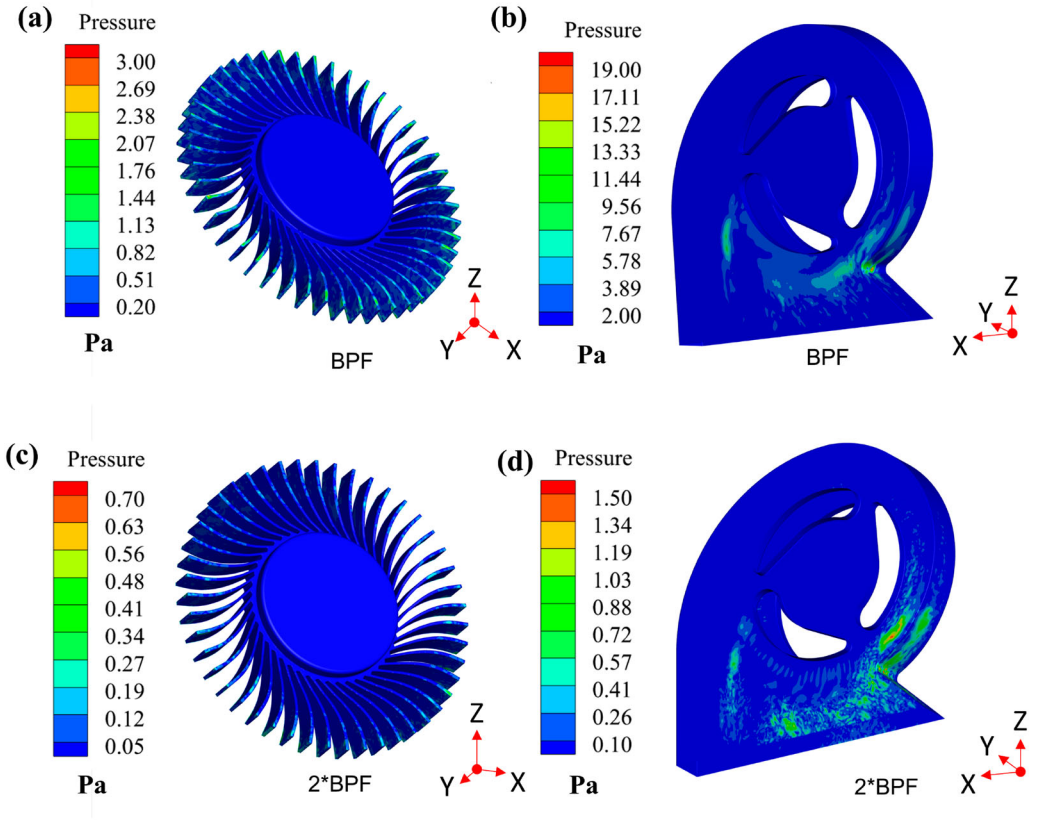

Figure 15. (a) Pressure fluctuation distribution on the blade surface at BPF (b) Pressure fluctuation distribution on the volute wall at BPF (c) Pressure fluctuation distribution on the blade surface at 2∗BPF (d) Pressure fluctuation distribution on the volute wall at 2∗BPF.

Figure 15 shows the pressure fluctuation of BPF and 2*BPF. The distribution indicates that the highest RMS pressure fluctuation occurs on the volute wall (as shown in Figure 15(b,d)), while the pressure fluctuation on the blade surface is minimal (as shown in Figure 15(a,c)), with amplitudes of only 3 Pa and 0.7 Pa at BPF and 2*BPF, respectively. Furthermore, the pressure fluctuation amplitude at BPF is much greater than at 2*BPF, suggesting that BPF is the primary frequency component. The highest pressure fluctuation at BPF is concentrated on the volute tongue area, reaching 19 Pa, while at 2*BPF, it is only 1.5 Pa, and the distribution pattern is more scattered compared to BPF. Specifically, the pressure fluctuation at 2*BPF is not only concentrated on the volute tongue but also scattered in the outlet region where flow turbulence is high.

In addition to the BPF and its harmonics, the RF and its harmonic components also exhibit prominent peaks in the turbulent energy spectrum. Figure 16 presents the corresponding distribution contours on the blade and volute wall. The RF and its higher harmonic distributions exhibit similar patterns, with maximum values concentrated around the blade tip and the outlet region of the volute wall. Furthermore, the hub plane of the volute wall

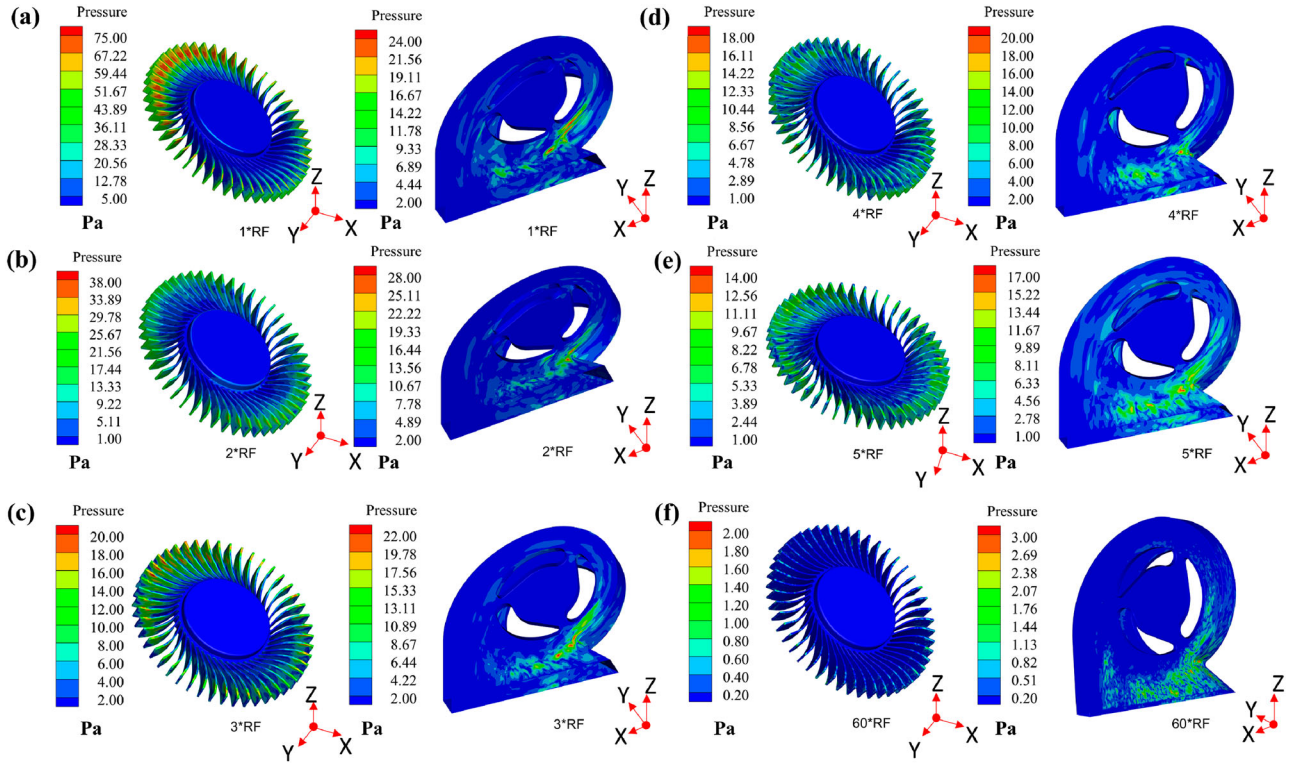

Figure 16. Pressure fluctuation on the blade surface and volute wall at the frequency (a) RF (b) 2∗RF (c) 3∗RF (d) 4∗RF (e) 5∗RF (f) 60∗RF.

demonstrates a broader distribution of pressure fluctuations compared to the shroud plane. This observation is consistent with the transient analysis of the boundary layer behaviour.

At RF and 2*RF shown in Figures 16(a,b), the pressure fluctuation amplitude on the blade surface is greater than that on the volute wall. Especially at RF, the maximal pressure fluctuation in the blade surface reaches 75 Pa, which is almost three times larger than that on the volute wall. Until the frequency goes up to 3*RF in Figure 16(c), the maximal pressure fluctuation on the blade surface is equal to that on the volute wall, which are both approximately 20 Pa. At the higher harmonic components in Figure 16(d–e), the pressure fluctuation amplitude on the volute wall exceeds that on the blade surface, especially on BPF in Figure 16(f), the maximal pressure fluctuation on the volute wall is six times larger than that on the blade surface. At 60*RF, pressure fluctuation on the blade surface is weak while pressure fluctuation on the volute wall is still strong, from which we can deduce the high-frequency components of dipole sound mainly come from the pressure fluctuation on the volute wall.

6. Conclusion

The internal flow field of an ultrathin centrifugal fan used for forced cooling in laptops is thoroughly analyzed. Particular emphasis is placed on the study of flow separation and boundary layer effects, with their contributions to flow losses evaluated through entropy production analysis. The entropy production is decomposed into terms associated with molecular viscosity and eddy viscosity, facilitating the differentiation between regions where distinct flow processes occur. Furthermore, the turbulent characteristics are investigated using hot-wire anemometry, while surface pressure fluctuations are examined in the frequency domain. Based on these analyses, several conclusions are drawn:

(1) The boundary layer thickness reaches 0.8 mm in both ends which makes up 10% of the total height of the volute, which is nonnegligible; Through the Q criterion and wall shear stress analysis, flow separation presents non-uniformity in the circumferential direction and axial direction in the blade passage; Through entropy production analysis, the boundary layer is the main source of entropy production and makes up 96% of the total entropy production;
(2) The pressure fluctuation on volute wall mainly concentrated on volute tongue area and the wall near outlet, while the pressure fluctuation on blade surface is mainly distributed on the suction surface where flow separation occurs. The BPF and RF and its higher frequency harmonics of the pressure fluctuation are mainly distributed on the blade tip area

and hub plane of the volute wall. With the frequency increasing, the contribution of pressure fluctuation on the volute wall is growing.

Through simulation and experimental measurement, the internal flow field is validated to be quite complex. The investigation into the flow characteristics of the ultrathin centrifugal fan is crucial for the development of a quiet and highly efficient cooling fan.

Disclosure statement

No potential conflict of interest was reported by the author(s).

Funding

This research has been supported by the Open Fund of Science and Technology on Thermal Energy and Power Laboratory (No. TPL 2022B02) and the National Natural Science Foundation of China (No.52076086).

Data availability statement

The data that support the findings of this study are available from the corresponding author upon reasonable request.

References

Amer, M. (2023). A novel bionic impeller for laptop cooling fan system. *Results in Engineering*, *20*, 101558. https://doi.org/10.1016/j.rineng.2023.101558

Amer, M. (2024). An innovative noise reduction blower fan housing design used in electronics cooling. *Measurement: Energy*, *1*, 100002.

Borcherding, T., Bode, C., Rosenzweig, M., Przytarski, P. J., Leggett, J., & Sandberg, R. D. (2023). Entropy loss breakdown comparison for LES and RANS of a transonic compressor stage midspan section. In *Volume 13A: Turbomachinery – Axial Flow Fan and Compressor Aerodynamics* (pp. V13AT29A032). American Society of Mechanical Engineers.

Deng, Q., Pei, J., Wang, W., & Sun, J. (2023). Investigation of energy dissipation mechanism and the influence of vortical structures in a high-power double-suction centrifugal pump. *Physics of Fluids*, *35*(7), 075147. https://doi.org/10.1063/5.0157770

Denton, J. D. (1993). Loss mechanisms in turbomachines. In *Volume 2: Combustion and Fuels; Oil and Gas Applications; Cycle Innovations; Heat Transfer; Electric Power; Industrial and Cogeneration; Ceramics; Structures and Dynamics; Controls, Diagnostics and Instrumentation; IGTI Scholar Award* (pp. V002T14A001). American Society of Mechanical Engineers.

Denton, J., & Pullan, G. (2012). A numerical investigation into the sources of Endwall loss in axial flow turbines. In *Turbomach. Parts B C* (Vol. 8, pp. 1417–1430). American Society of Mechanical Engineers.

Fan, B., Liang, Z., Fan, R., & Chen, S. (2022). Numerical study on entropy generation of the multi-stage centrifugal pump. *Entropy*, *24*, 923. https://doi.org/10.3390/e24070923

Fehse, K. R., & Neise, W. (1999). Generation mechanisms of low-frequency centrifugal fan noise. *AIAA Journal*, *37*(10), 1173–1179. https://doi.org/10.2514/2.610

Fritsche, M., Epple, P., & Delgado, A. (2022). Numerical and theoretical investigation of the gap flow in centrifugal fans for design and off-design conditions. *Journal of Fluids Engineering*, *145*(3), 031203. https://doi.org/10.1115/1.4056311

Grace, S. M. (2015). Fan broadband interaction noise modeling using a low-order method. *Journal of Sound and Vibration*, *346*, 402–423. https://doi.org/10.1016/j.jsv.2015.02.013

Guan, H., Jiang, W., Yang, J., Wang, Y., Zhao, X., & Wang, J. (2020). Energy loss analysis of the double-suction centrifugal pump under different flow rates based on entropy production theory. *Proceedings of the Institution of Mechanical Engineers Part C-Journal of Mechanical Engineering Science*, *234*(20), 4009–4023. https://doi.org/10.1177/0954406220919795

He, G.-W., Rubinstein, R., & Wang, L.-P. (2002). Effects of subgrid-scale modeling on time correlations in large eddy simulation. *Physics of Fluids*, *14*(7), 2186–2193. https://doi.org/10.1063/1.1483877

Herwig, H., & Kock, F. (2006). Direct and indirect methods of calculating entropy generation rates in turbulent convective heat transfer problems. *Heat Mass Transfer*, *43*(3), 207–215. https://doi.org/10.1007/s00231-006-0086-x

Hofer, D., Krieger, M., & Kirchhofer, M. (2021). Particle image velocimetry and constant temperature anemometer measurements of the jet produced by a centrifugal fan. *Physics of Fluids*, *33*(6), 065126. https://doi.org/10.1063/5.0052280

Jiang, B., Huang, Y., Yang, X., Xiao, Q., Yang, W., & Wang, J. (2022). Large eddy simulation on the vortex evolution in a squirrel-cage fan based on a slice computational model. *Engineering Applications of Computational Fluid Mechanics*, *16*(1), 1324–1343. https://doi.org/10.1080/19942060.2022.2086621

Kim, M., Lim, J., Kim, S., Jee, S., & Park, D. (2020). Assessment of the wall-adapting local eddy-viscosity model in transitional boundary layer. *Computer Methods in Applied Mechanics and Engineering*, *371*, 113287. https://doi.org/10.1016/j.cma.2020.113287

Kock, F., & Herwig, H. (2004). Local entropy production in turbulent shear flows: A high-reynolds number model with wall functions. *International Journal of Heat and Mass Transfer*, *47*(10), 2205–2215. https://doi.org/10.1016/j.ijheatmasstransfer.2003.11.025

Kock, F., & Herwig, H. (2005). Entropy production calculation for turbulent shear flows and their implementation in cfd codes. *International Journal of Heat and Fluid Flow*, *26*(4), 672–680. https://doi.org/10.1016/j.ijheatfluidflow.2005.03.005

Lewis, D., Moreau, S., Jacob, M. C., & Sanjosé, M. (2023). Large eddy simulation of the ACAT1 fan stage for broadband noise prediction. *Journal of Sound and Vibration*, *565*, 117888. https://doi.org/10.1016/j.jsv.2023.117888

Liu, X., Farhat, M., & Li, Y. L. (2022). Onset of flow separation phenomenon in a low-specific speed centrifugal pump impeller. *Journal of Fluids Engineering*, *145*(2), 021206. https://doi.org/10.1115/1.4056213

Marconcini, M., Pacciani, R., Arnone, A., Michelassi, V., Pichler, R., Zhao, Y., & Sandberg, R. (2019). Large eddy simulation and RANS analysis of the end-wall flow in a linear low-pressure-turbine cascade–part II: Loss generation. *Journal of Turbomachinery*, *141*(5), 051004. https://doi.org/10.1115/1.4042208

Nguyen, T., King, S., & Hassan, Y. (2021). Experimental investigation of turbulent characteristics in pore-scale regions of porous media. *Experiments in Fluids*, *62*(4), 72. https://doi.org/10.1007/s00348-021-03171-1

Ottersten, M., Yao, H.-D., & Davidson, L. (2021). Tonal noise of voluteless centrifugal fan generated by turbulence stemming from upstream inlet gap. *Physics of Fluids*, *33*(7), 075110. https://doi.org/10.1063/5.0055242

Ren, K. X., Shuai, Z. J., Wang, X., Jian, J., Yu, T., Dong, L. Y., Li, W. Y., & Jiang, C. X. (2022). Aerodynamic noise prediction of a high-speed centrifugal fan considering impeller-eccentric effect. *Physics of Fluids*, *35*(7), 075147.

Sandberg, R. D., & Michelassi, V. (2022). Fluid dynamics of axial turbomachinery: Blade- and stage-level simulations and models. *Annual Review of Fluid Mechanics*, *54*(1), 255–285. https://doi.org/10.1146/fluid.2022.54.issue-1

Sorguven, E., Incir, S., & Highgate, J. (2022). Understanding loss generation mechanisms in a centrifugal pump using large eddy simulation. *International Journal of Heat and Fluid Flow*, *96*, 108994. https://doi.org/10.1016/j.ijheatfluidflow.2022.108994

Tang, X., Jiang, W., Li, Q., Hou, G., Zhang, N., Wang, Y., & Chen, D. (2022). Analysis of hydraulic loss of the centrifugal pump as turbine based on internal flow feature and entropy generation theory. *Sustainable Energy Technologies and Assessments*, *52*, 102070. https://doi.org/10.1016/j.seta.2022.102070

Tucker, P. G. (2011). Computation of unsteady turbomachinery flows: Part 1–progress and challenges. *Progress in Aerospace Sciences*, *47*(7), 522–545. https://doi.org/10.1016/j.paerosci.2011.06.004

Tucker, P. G. (2011). Computation of unsteady turbomachinery flows: Part 2–LES and hybrids. *Progress in Aerospace Sciences*, *47*(7), 546–569. https://doi.org/10.1016/j.paerosci.2011.07.002

Walsh, P. A., Walsh, E. J., & Grimes, R. (2010). Viscous scaling phenomena in miniature centrifugal flow cooling fans: Theory, experiments and correlation. *Journal of Electronic Packaging*, *132*(2), 021001. https://doi.org/10.1115/1.4001590

Xu, C., Du, Z., Mao, Y., Zhao, Y., Zhao, W., & Li, M. (2024). Sources and mechanisms of flow loss and hydroacoustics in a pre-swirl stator pump-jet propulsor. *Physics of Fluids*, *36*(2), 025158. https://doi.org/10.1063/5.0192405

Xu, W., Chen, G., Shi, H., Zhang, P., & Chen, X. (2023). Research on operational characteristics of coal power centrifugal fans at off-design working conditions based on flap-angle adjustment. *Energy*, *284*, 129363. https://doi.org/10.1016/j.energy.2023.129363

Yadegari, M., & Bak Khoshnevis, A. (2020). Entropy generation analysis of turbulent boundary layer flow in different curved diffusers in air-conditioning systems. *The European Physical Journal plus*, *135*(6), 534. https://doi.org/10.1140/epjp/s13360-020-00545-y

Zaheer, S. Q., & Disimile, P. J. (2021). Flow field analysis and nearfield acoustic signature reduction of a stationary fan blade array. *Journal of Fluids Engineering*, *143*(4), 041203. https://doi.org/10.1115/1.4049116

Zhang, L., Kritioti, L., Wang, P., Zhang, J., & Zangeneh, M. (2022). A detailed loss analysis methodology for centrifugal compressors. *Journal of Turbomachinery*, *144*(5), 051013. https://doi.org/10.1115/1.4054065

Zhao, Y., & Sandberg, R. D. (2020). Using a new entropy loss analysis to assess the accuracy of RANS predictions of an high-pressure turbine vane. *Journal of Turbomachinery*, *142*(8), 081008. https://doi.org/10.1115/1.4046531

Zheng, S., Chen, J., Li, Y., & Chai, M. (2023). Flow characteristics of a centrifugal fan with optimized edge curvatures of an impeller front disk. *Proceedings of the Institution of Mechanical Engineers Part A-Journal of Power and Energy*, *237*(10), 095765.

Zhou, S., Deng, H., Ma, Y., & Zhang, S. (2019). Investigation on the performance of forward bending fan. *International Journal of Turbo & Jet-Engines*, *36*(2), 207–217.

Zhou, L., Hang, J., Bai, L., Krzemianowski, Z., El-Emam, M. A., Yasser, E., & Agarwal, R. (2022). Application of entropy production theory for energy losses and other investigation in pumps and turbines: A review. *Applied Energy*, *318*, 119211. https://doi.org/10.1016/j.apenergy.2022.119211